
Title	Green synthesis of vertical graphene nanosheets and its application in high-performance supercapacitors
Author(s)	Bo Ouyang, Yongqi Zhang, Zheng Zhang, Hong Jin Fan and R. S. Rawat
Source	<i>RSC Advances</i> , 6(28), 23968-23973
Published by	Royal Society of Chemistry

Copyright © 2016 Royal Society of Chemistry

This is the author's version (post-print) of a work that was accepted for publication in the following source:

Ouyang, B., Zhang, Y., Zhang, Z., Fan, H. J., & Rawat, R. S. (2016). Green synthesis of vertical graphene nanosheets and their application in high-performance supercapacitors. *RSC Advances*, 6(28), 23968-23973. <http://dx.doi.org/10.1039/C5RA27084G>

Notice: Changes introduced as a result of publishing processes such as copy-editing and formatting may not be reflected in this document. For a definitive version of this work, please refer to the published source:

Green synthesis of vertical graphene nanosheets and its application in high-performance supercapacitors

Bo Ouyang^a; Yongqi Zhang^b; Zheng Zhang^c; Hong Jin Fan^b; R. S. Rawat^{a*}

^aNatural Sciences and Science Education, National Institute of Education, Nanyang
Technological University, 637616, Singapore

^bSchool of Physics and Mathematics Science, Nanyang Technological University, 637371,
Singapore

Institute of Materials Research and Engineering, A*STAR (Agency for Science, Technology and
Research), 3 Research Link, Singapore 117602

* Corresponding author

The email address: rajdeep.rawat@nie.edu.sg (R. S. Rawat)

Telephone: (+65) 67903908

Abstract

Vertical standing graphene sheets are highly desirable in energy storage applications because without π - π stacking their surface can be fully utilized. In this work, vertical graphene nanosheets (VGS) is successfully synthesized on the nickel foam via a simple plasma enhanced chemical vapor deposition (PECVD) technique. Instead of hazardous and costly hydrocarbon gases, we adopt a green approach by using a low-cost, non-toxic, sustainable and environmentally-friendly natural organic material, *M. alternifolia* essential oil (containing hydrocarbon monomer), as the precursor. The 4 minute deposition duration results in multilayered horizontal graphene (h-GS) with sparsely distributed vertical graphene while 16 minute deposition leads to fully covered vertical graphene nanosheets (f-VGS). To demonstrate their application as conductive and high-surface-area substrate in energy storage, MnO₂ thin films are hydrothermal grown to form MnO₂@f-VGS core-shell structure and MnO₂@h-GS. The core@shell electrode of MnO₂@f-VGS demonstrates a significantly higher specific capacitance of 203 F g⁻¹ at a current density of 10 A g⁻¹ compared to that of 82 F g⁻¹ at 10 A g⁻¹ shown by MnO₂@h-GS. Moreover, the assembled full supercapacitors containing MnO₂@f-VGS || active carbon as electrodes can deliver a reasonably high specific capacitance of 250 F g⁻¹ at 2 A g⁻¹. Such f-VGS may have application also in battery and fuel cell electrodes.

1. Introduction

Due to continuously increasing demand for energy storage, supercapacitors have received remarkable attention because of their distinct advantages such as high power density, long lifetime and ultrafast charge and discharge capability ^{1, 2}. Therefore, carbon based materials including carbon nanotubes (CNT), activated carbon, graphene and carbon nanofibers have attracted worldwide research interest and gradually become the most promising electrode materials due to their cost-efficiency, high chemical stability and excellent conductivity ³⁻⁶. Until now, there have been significant efforts concentrating on the synthesis of chemically exfoliated graphene oxide (GO) with high surface area for anchoring enhanced amount of active materials on the surface ⁷. However, such material will inevitably suffer from low conductivity and insufficient ionic diffusion because of surface defects and large amounts of oxygen-containing functional groups introduced during the oxidation process of graphite, severely limiting their application in energy storage devices ⁷. Even after the reduction of GO, the reduced graphene oxide (rGO) is still less conductive than the pristine graphene ⁸. Additionally, the hydrophobic rGO sheets are considerably easy to restack and aggregate because of the partial removal of hydrophilic functional groups after reducing GO, which extensively decreases its specific surface area and hence lowers the corresponding performance.

Recently, vertical graphene nanosheets (VGS) have shown considerable potential due to their high electrical conductivity, large surface to volume ratio, open network structure with graphene flakes oriented perpendicularly to the electrode surface, in contrast to the horizontal graphene⁹. Such structures are desired to significantly increase the capacitive mechanism of charge storage by enhanced ion diffusivity and ion accessibility¹⁰. Actually, previous studies have demonstrated that VGS-based electrodes exhibited unexpectedly high power density and stable performance¹¹,¹². Nevertheless, so far VGS are usually produced by hazardous, expensive purified hydrocarbon gases, which extensively impedes the further utilization for various applications¹³. Moreover, C₂F₆, the commonly used carbon precursor for the production of VGS, leads to non-conductive fluorocarbon layer formation on the substrate, inevitably resulting in the increased electrical resistance and lower capacitance within electrode materials^{14, 15}. Although Seo DH synthesized VGS through environmentally-benign natural precursor butter, the complicated components within the butter (mostly consisting of butterfat, milk proteins and water) are expected to form other chemical bonding in VGS, making it less suitable for further investigation and application in supercapacitor¹².

We have recently reported the catalyst free plasma enhanced growth of graphene from sustainable source, tea tree oil (*Melaleuca alternifolia* extract), on silicon substrate with strong potential for use in resistive random access memory (RRAM)¹⁶. It may be highlighted that there

are several efforts to introduce simple green processes using a wide variety of precursors that include food materials such as butter ¹², honey ¹⁷, eggs ¹⁸, cookies ¹⁹, table sugar ²⁰, natural and plastic waste ¹⁹, and other solid carbon sources ²¹. Most of these materials are easily available but the scalability and sustainability of graphene synthesis using these precursors is not trivial or rather questionable. Our interest is to further develop the simple sustainable pathway of using easily renewable monomer of *Melaleuca alternifolia* extract in radio frequency (RF) PECVD system to synthesize high quality vertical graphene in relatively short time and demonstrate their suitability for various applications including energy storage. The *M. alternifolia* extract is a sustainable and abundant commercial resource, obtained by distillation of leaves of commonly known tea-tree, which is volatile at room temperature under vacuum conditions allowing easy admittance of its vapors in deposition chamber. In present work, we extend the same simple and cost-efficient RF PECVD based approach ¹⁶ to directly fabricate VGS on porous nickel foam using the same sustainable source of tea tree oil and demonstrate its applications in supercapacitors.

Furthermore, by controlling deposition duration, the optimized fully covered VGS (f-VGS) with large specific surface area and large amount of reactive edges is obtained, leading to enhanced supercapacitive performance of as-synthesized composites. In comparison, corresponding composite of multilayer horizontal graphene (h-GS) results in lower overall performance, which

demonstrates the superior functionalization of f-VGS compared with that of h-GS. Moreover, the stable and synergistic integration of metal oxide nano-architecture to f-VGS is achieved by hydrothermal deposition of MnO₂ film and an asymmetric supercapacitor is successfully constructed by coupling MnO₂@f-VGS as anode and active carbon as cathode for practical application. Our results show that the f-VGS derived from natural oil gives rise to the very reliable and promising performance, leading to the next generation supercapacitors.

2. Experimental

2.1. Growth of VGS

The VGS was synthesized using our home-made PECVD system as shown in Fig. 1. In a typical deposition process, commercial Ni foam (1×1 cm) was placed into the quartz tube reactor at about 15 cm from the left radio frequency electrode. Afterwards, the quartz tube reactor was pumped to vacuum of 3.0 Pa. With the pressure kept below 10 Pa, the quartz tube reactor was heated to 800 °C under hydrogen (100 sccm) flow. Hydrogen plasma was produced by Caeser136 RF generator (500 W, 13.56 MHz) to further clean the Ni foam substrate. Then, a small amount of essential oil vapor was introduced into the reactor tube at ambient temperature. The 500 W RF plasma discharge was applied to efficiently obtain the carbon radicals from the essential oil vapors for graphene synthesis. h-GS anchored on the surface of nickel foam was

achieved through plasma treatment of 4 min, while f-VGS anchored on substrate surface was obtained through plasma treatment of 16 min. After the completion of plasma discharge duration, the samples were rapidly cooled down to room temperature, under background vacuum pressure, at cooling rate of $\sim 70\text{ }^{\circ}\text{C min}^{-1}$.

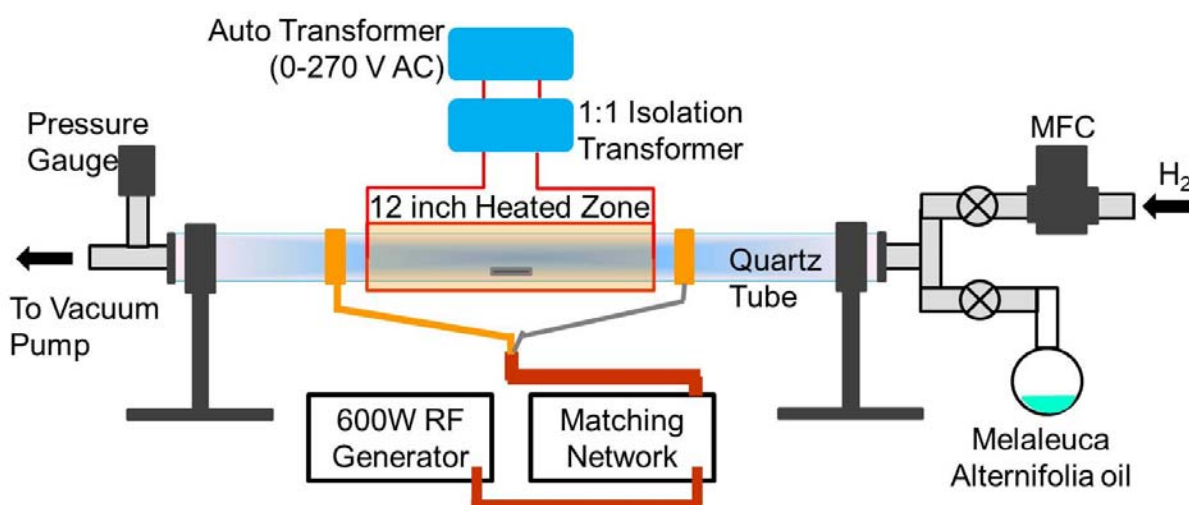


Fig. 1: Schematic diagram of home-made RF PECVD system for the growth of the VGS.

2.2. Synthesis of MnO_2 @f-VGS and MnO_2 @h-GS

MnO_2 nanostructures anchored f-VGS/h-GS composites were fabricated by hydrothermal approach. In brief, the KMnO_4 solution was prepared by dissolving KMnO_4 (0.1106 g) into distilled water (35 mL). The resulting solution was then transferred into Teflon-lined stainless steel autoclave. One piece of as-prepared f-VGS/h-GS were immersed into the reaction solution respectively. The autoclave was then sealed and the hydrothermal reaction was performed at $150\text{ }^{\circ}\text{C}$ for 1.2 h. The autoclave was then cooled down to room temperature, the samples were

rinsed with DI water for several times and dried overnight under vacuum at 60 °C, the loading density of active materials in MnO₂@f-VGS and MnO₂@h-GS are about 1.3 mg cm⁻² and 1 mg cm⁻², respectively.

2.3. Characterization

Field-emission scanning electron microscopy (FESEM) analysis was conducted by JEOL JSM-6700F scanning electron microscope with an accelerating voltage of 10 kV. Transmission electron microscopy (TEM) measurements were performed by JEOL-2010 UHR high resolution transmission electron microscope with an accelerating voltage of 200 kV. X-ray photoelectron spectroscopy (XPS) analysis was conducted using VG ESCALAB 220i-XL XPS with a monochromatic Al K α (1486.7 eV) X-ray source. Binding energy of C1s peak from sp²-bonded carbon at 284.5 eV is used as a reference for correction. Raman spectra were obtained using a WITEC CRM200 Raman system with 532 nm excitation laser. X-ray powder diffraction (XRD) pattern was collected using a D8 advanced diffractometer with Cu K α line ($\lambda = 0.154056$ nm). The electrochemical properties of the electrodes were measured in 0.1 M Na₂SO₄ electrolyte using three electrodes cell configuration (CHI6604D, Shanghai Chenhua).

2.4. Calculation of specific capacitance

Single electrode calculation:

Specific capacitances of the single electrodes were according to the following equation (by CV data):

$$C_s = \frac{Q}{\Delta V \cdot m} \quad (1)$$

where C_s ($F \text{ g}^{-1}$) is specific capacitance, Q (C) is the average charge during the charging and discharging process, ΔV (V) is the potential window and m (g) is the total mass of the active material of the electrode.

Alternatively, specific capacitances of electrodes were obtained by galvanostatic charge-discharge method based on the following equation:

$$C_s = \frac{I \cdot \Delta t}{\Delta V \cdot m} \quad (2)$$

where C_s ($F \text{ g}^{-1}$) is the specific capacitance, I (A) is the constant discharging current, Δt (s) is the discharging time, ΔV (V) is the potential window, m (g) is the total mass of the active material of the electrode.

Packaged full cell

For asymmetric capacitors, one must have mass balance based on charge equivalence on both electrodes according to the following equation:

$$\frac{m_+}{m_-} = \frac{C_- V_-}{C_+ V_+} \quad (3)$$

where m_+ is total mass of positive electrode and m_- is the total mass of negative electrode. The $C_{s,cell}$ is the overall specific capacitance of the device. C_- and C_+ are specific capacitances of individual electrodes. V_+ and V_- represent potential window of individual electrode.

Therefore, the specific capacitance of the device can be evaluated from the discharging curve according to the following equation:

$$C_{s,cell} = \frac{I}{dV/dt} \left(\frac{1}{m_+} + \frac{1}{m_-} \right)$$

3. Results and discussion

Fig. 2a-d exhibit the representative SEM and FESEM images of h-GS and f-VGS respectively, where uniform and dense nano-architecture of f-VGS deposition is observed in Fig. 2c-d with fully covered VGS on surface of the graphite-type flake for 16 minute deposition, compared with separated seldom VGS architectures on mostly horizontal multilayer graphene of h-GS for 4 minute deposition seen in Fig. 2a-b. As shown in Fig. 2b, most of the outer surface of Ni foam is covered by multilayer horizontal graphene architecture with little amount of VGS nanostructure, which has been investigated by our previous report²². The VGS nano-architecture is desirable as it possess remarkable conductivity because of large surface area and large amount of edges. The image in Fig. 2e, shows the nanosheets of VGS with exposed reactive edges and curl configuration, which is associated with equilibrium of attachment and detachment rate of carbon

adatoms. Such “open” edges are favorable for electrical conduction from the substrate, leading to enhanced potential in electron transfer. Moreover, the spacing between graphene layers is measured as ~ 0.34 nm, corresponding to the graphite (002) planes of graphene structures (Fig. 2f).

Fig. 3 shows the FESEM images of $\text{MnO}_2@h\text{-GS}$ and $\text{MnO}_2@f\text{-VGS}$. As shown in Fig. 3a-b, MnO_2 nanocrystals on h-GS have relatively subdued perpendicular architecture because of a few VGS on h-GS substrate, which severely decreases the overall specific surface area and therefore lower the overall performance. In comparison, Fig. 3c-d shows MnO_2 thin film assembled by nanocrystals is uniformly and strongly orthogonally anchored on the surface of VGS on f-VGS surface. The corresponding 3D hierarchical composites (due to use of nickel foam) still hold the initial architecture of f-VGS, which could accelerate ion transfer and minimize remarkable structural rearrangements during electrochemical redox reaction. Based on this, f-VGS not only delivers a substrate with excellent conductivity, but also contributes to keep nano-architecture of active materials anchored on the surface. The well-defined MnO_2 thin film in Fig. 3d is able to achieve highly microporous structure as well as effective contact with VGS. Moreover, TEM is used to confirm the nano-structure of as-synthesized $\text{MnO}_2@f\text{-VGS}$ composites (Fig. 3e), which demonstrates that MnO_2 nanodomains are randomly dispersed throughout the body of VGS. HRTEM (Fig. 3f) further exhibits the lattice spacings of 0.69, 0.31 and 0.35 nm, corresponding

to (110), (310) and (220) planes of α -MnO₂ (International Centre for Diffraction Data (ICDD) number 00-044-0141), respectively. The above results not only depict the nano-structure of as-prepared composites, but also demonstrate that highly microporous architecture of f-VGS are still preserved after deposition of MnO₂.

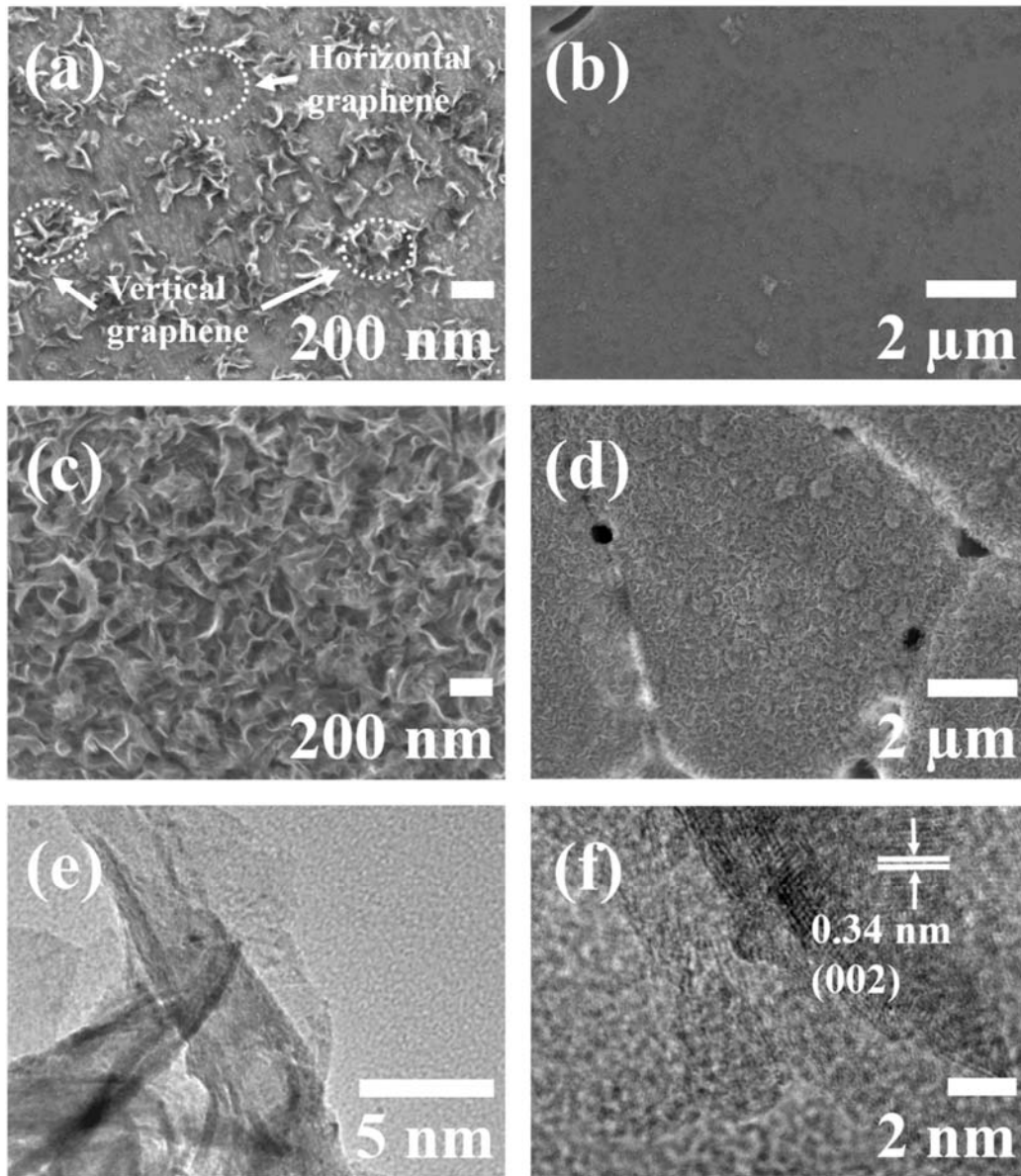


Fig. 2: (a) and (b) FESEM images of h-GS; (c) and (d) FESEM images of f-VGS; (e) and (f) TEM and HRTEM image and HRTEM of f-VGS.

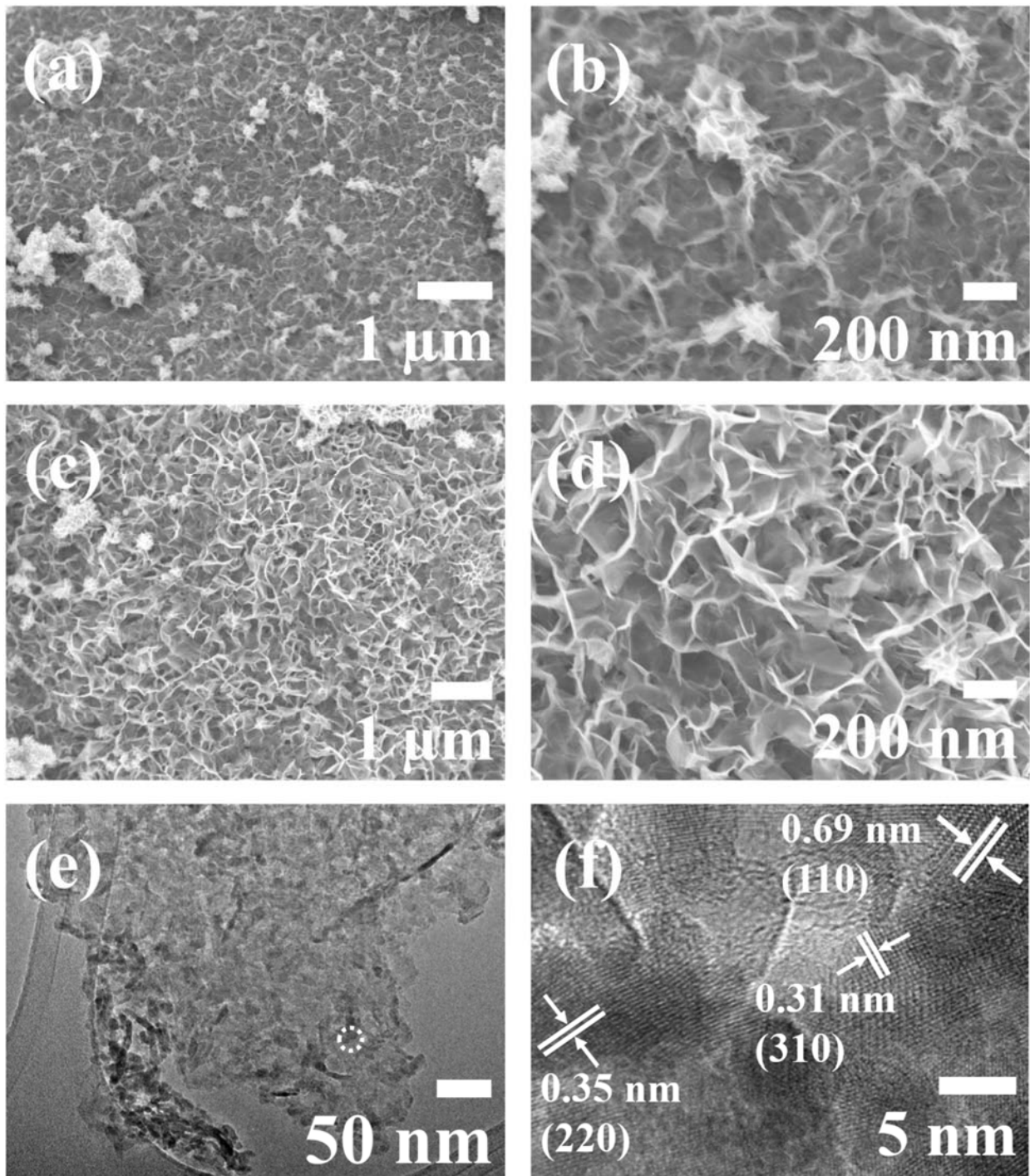


Fig. 3: (a) and (b) FESEM images of MnO₂@h-GS; (c) and (d) FESEM images of MnO₂@f-VGS; and (e) and (f) TEM and HRTEM images of MnO₂@f-VGS.

Fig. 4a shows the Raman spectra of h-GS, f-VGS and MnO₂@f-VGS respectively. Three characteristic Raman peaks, namely D, G and 2D, are clearly observed in f-VGS and h-GS spectra. The sharp D-band ($\sim 1360\text{ cm}^{-1}$) and D'-band peaks (shown in deconvoluted peak at $\sim 1630\text{ cm}^{-1}$) in Raman spectrum of f-VGS and h-GS, indicate a nanocrystalline architecture and the presence of large number of graphene defects and edges, exhibiting characteristics of VGS on both samples. The ratio of I_D/I_G in f-VGS is ~ 1.59 , much higher than that of h-GS (~ 1.05), which indicates much more amount of defects in f-VGS sample²³. This also demonstrates that much less number of VGS on the surface of h-GS sample, confirming FESEM results. The ratio of I_{2D}/I_G in h-GS and f-VGS are estimated to be ~ 0.17 and 0.21 respectively, suggesting multi-layer configurations²⁴. It can be seen that the well-defined Raman peaks of MnO₂ appears between 200 and 800 cm^{-1} after MnO₂ deposition on the surface of f-VGS substrate for MnO₂@f-VGS sample. Meanwhile, the representative peaks of f-VGS still remain unchanged, suggesting that the hierarchical nano-architecture of f-VGS is not altered during hydrothermal approach.

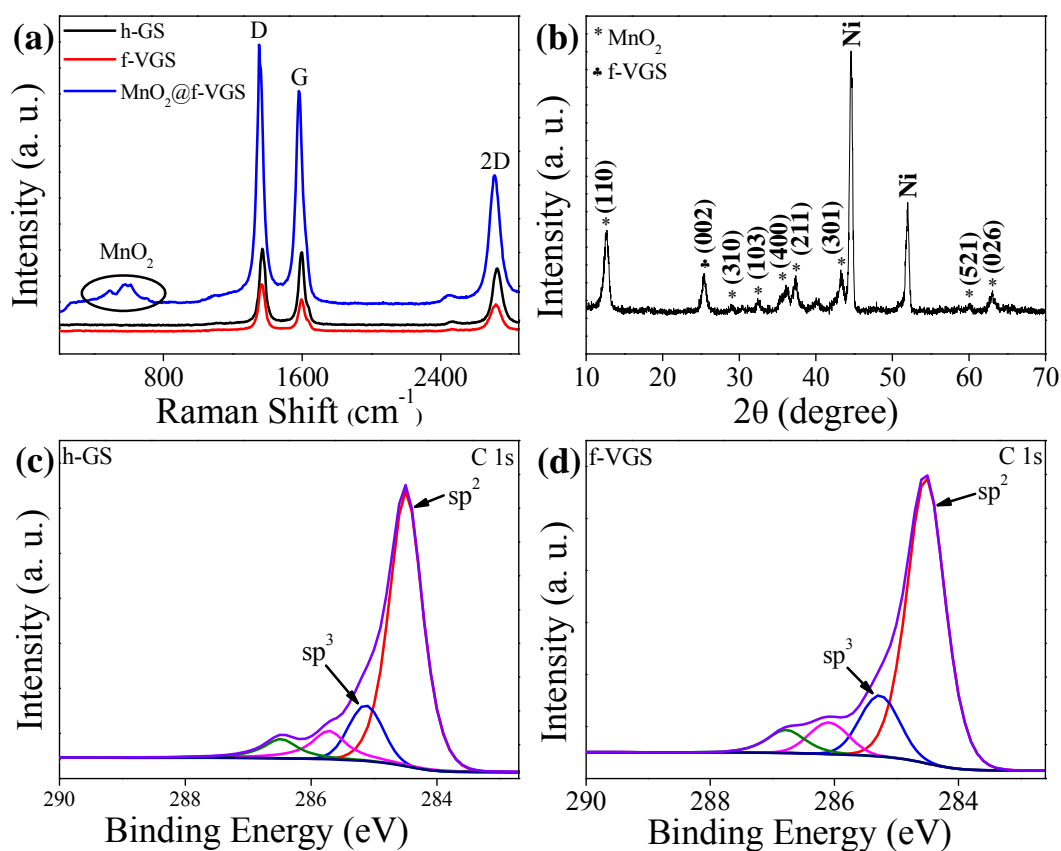


Fig. 4: (a) Raman spectra of MnO₂@f-VGS, f-VGS and h-GS; (b) XRD pattern of MnO₂@f-VGS; (c) XPS spectra of C 1s peaks of h-GS; (d) XPS spectra of C 1s peaks of f-VGS.

Fig. 4b exhibits the XRD patterns of the MnO₂@f-VGS. The characteristic diffraction peak at 26.5°, corresponding to the (002) reflections of graphitic carbon (JCPDS card no. 75-1621), is due to f-VGS component in composite. Meanwhile, other diffraction peaks, marked with ‘*’, correspond well with tetragonal cryptomelane type MnO₂ (JCPDS No. 29-1020). The peaks corresponding to Ni foam are also observed in diffraction pattern. The presence of sp² and sp³-bonded carbon in h-GS and f-VGS is further confirmed by XPS measurements (Fig. 4c-d). In the

XPS C1 spectrum, two peaks at binding energies of 284.5 and 285.3 eV corresponding to the sp^2 and sp^3 carbon components, respectively, are observed. As estimated from Fig. 4c and 4d, the amount of sp^2 and sp^3 -bonded carbon in h-GS is about 63.4% and 9.4%, respectively, lower than the corresponding values of 71.0% and 15.2%, respectively in f-VGS, demonstrating much enhanced ratio of edge-like component in f-VGS due to significantly enhanced proportion of VGS. The detection of oxygen in XPS spectrum may be associated with the presence of oxygen-containing compounds, such as terpinen-4-ol ($C_{10}H_{18}O$, 30~48%) and 1,8-cineole ($C_{10}H_{18}O$, 0~15%) as primary components, in *M. alternifolia* essential oil used in present study as carbon source.

The supercapacitive performances of $MnO_2@h-GS$ and $MnO_2@f-VGS$ are evaluated in a three electrode cell configuration. As shown in Fig. 5a, both cyclic voltammetry (CV) curves exhibit typically symmetrical rectangular shapes at the scan rate of 50 mV s^{-1} . Such different evaluations apparently indicate the better supercapacitive behavior for $MnO_2@f-VGS$ composites. As shown in Fig. 5b, the galvanostatic discharge curves of $MnO_2@f-VGS$ sample present enhanced performance and limited voltage drop, which gives rise to an higher gravimetric capacitances of 290 F g^{-1} at 2 A g^{-1} and 203 F g^{-1} at 10 A g^{-1} , in stark comparison with that of $MnO_2@h-GS$ sample which delivers the gravimetric capacitance of 163 F g^{-1} and 82 F g^{-1} . Moreover, for all the tested current densities in the range of $1\text{-}20\text{ A g}^{-1}$, the specific capacitance of $MnO_2@f-VGS$

composite is significantly higher than that of $\text{MnO}_2@\text{h-GS}$ (more than twice at current densities $\geq 5 \text{ A g}^{-1}$) (Fig. 5c), which also confirm the enhanced synergistic effect of f-VGS compared to that of h-GS which has horizontal graphene with lesser amount of VGS. This indicates that an increase in amount of VGS on the substrate improves the overall capacitive performance of composites.

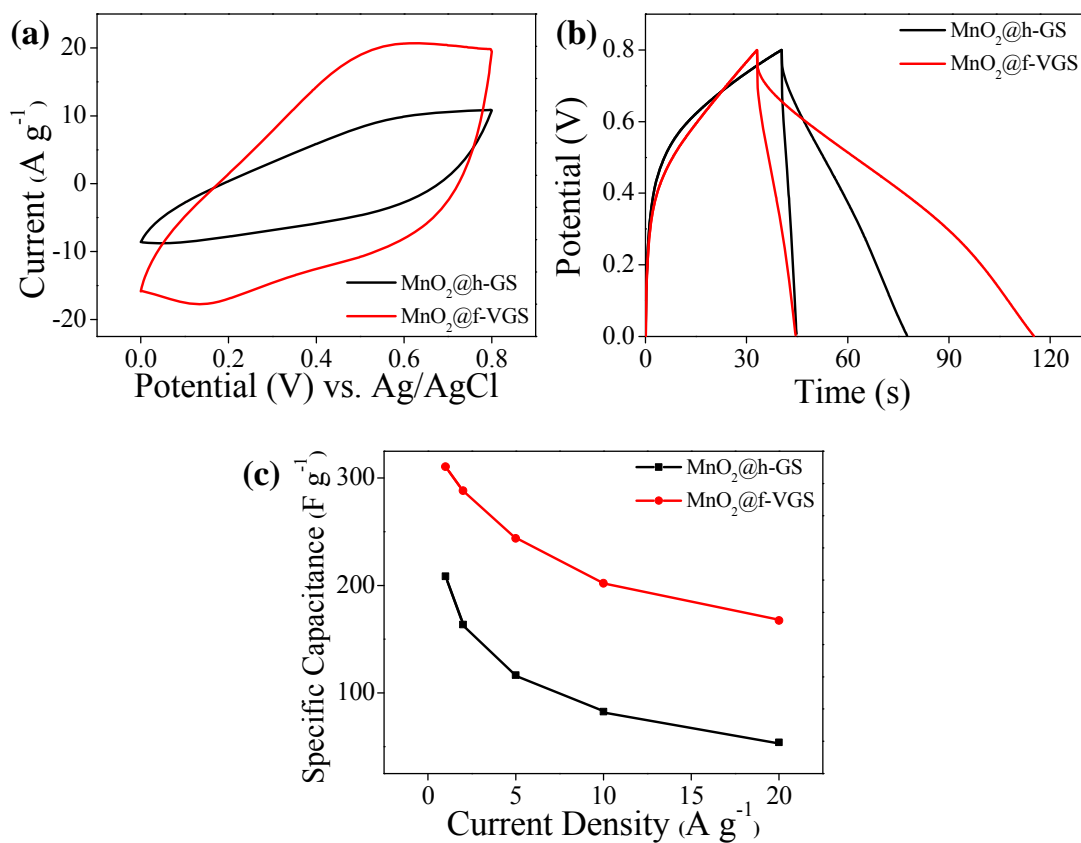


Fig. 5: (a) CV comparison at the scan rates of 50 mV s^{-1} ; (b) Galvanostatic discharge comparison at the current densities of 2 and 10 A g^{-1} ; (c) Galvanostatic charge-discharge capacitance at different discharge current densities.

An asymmetric supercapacitor of MnO₂@f-VGS || active carbon was assembled with MnO₂@f-VGS composite as cathode and active carbon as anode. 0.1 M Na₂SO₄ was applied as electrolyte and porous non-woven cloth was used as separator (Fig. 6a). Fig. 6a shows CV chart performed from 0 V to 1.6 V at different scan rates. Fig. 6b shows the GCD results at different discharging current densities. The reason for charging/discharging curves being asymmetrical, in Fig. 6b, is that the charging current density was kept constant at 5 A g⁻¹ and while the discharging current densities were varied from 1 A g⁻¹ to 20 A g⁻¹. The fixed charging current density of 5 A g⁻¹ is evident from the fact that the charging time is almost similar for all 5 curves shown in Fig. 6b. The discharges at higher current densities of 10 and 20 A g⁻¹ lead to faster discharging while the discharges at lower current densities of 1 and 2 A g⁻¹ resulted in slower discharging, causing the asymmetry in the charging/discharging curves for these discharging current densities. It may be noted that the discharging at 5 A g⁻¹ (blue curve) resulted in symmetric curve in Fig. 6b as both charging and discharging current density were at 5 A g⁻¹. Fig. 6c exhibits the curves, in which the device delivers higher C_{sp} values of 351 F g⁻¹, 312 F g⁻¹, 256 F g⁻¹, 238 F g⁻¹, 208 F g⁻¹ at discharge current densities of 1, 2, 5, 10, and 20 A g⁻¹ respectively. The specific capacitance decreases with the increase of current density because the higher current makes more active material insufficient in the redox reaction as the scan rate increases. These specific capacitance values are higher than the reported literatures. Shen et al.,²⁵ in 2010, reported that the specific

capacitances of MnO₂@GO are 216.0, 197.2, 141.5, and 111.1 F g⁻¹, respectively at the current densities of 150, 200, 500, and 1000 mA g⁻¹. About 51.4% of specific capacitance was retained when the current density increased from 150 to 1000 mA g⁻¹. Zheyue et al.²⁶ reported that the specific capacitances of MnO₂-ERGO are 422.5, 353.8, 280.6, and 228.8 F g⁻¹ at current densities of 1, 2, 5, and 10 A g⁻¹, respectively. About 54.2% of specific capacitance has been retained when the current density increased from 1 to 10 A g⁻¹. Lele et al.²⁷ reported the specific capacitances of 267 and 208 F g⁻¹ at 0.2 A and 10 A g⁻¹, respectively, with retention of 77%. Compared with that, our results show that the specific capacitances of MnO₂@f-VGS are 311 and 168 F g⁻¹ at 1 and 20 A g⁻¹, respectively, with the specific capacitance retention of 54.0%. Therefore, our results are comparable with other similar systems reported in the literature. Meanwhile, the capacitance of the device only has a slight decrease during the first 1000 cycles and retains considerable stability during the next 9000 cycles, in which the capacitive retention is 87.1% (Fig. 6d). The stability is better than those reported in the previous literatures²⁸.

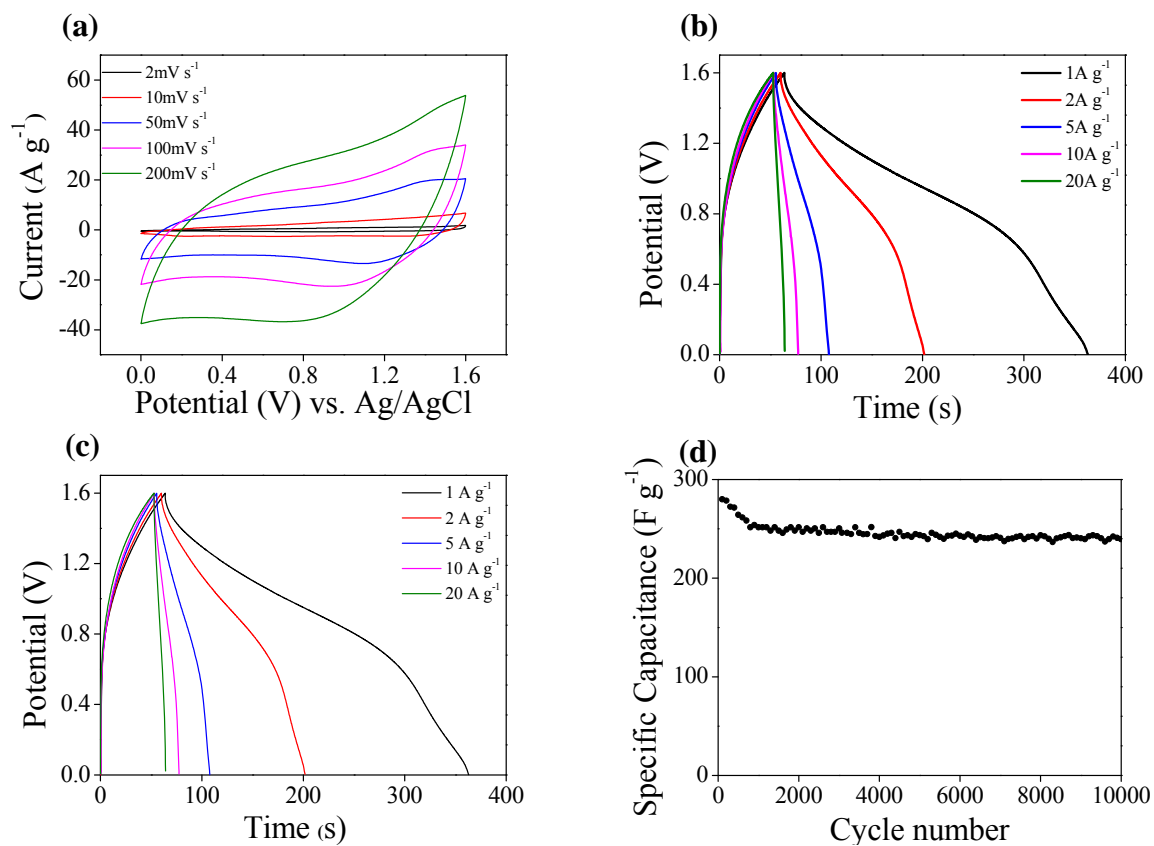


Fig. 6: (a) CV curves for the device at various scan rates; (b) Galvanostatic charge-discharge curves of the supercapacitor device at different discharge current densities; (c) specific capacitance of the supercapacitor device at different discharge current densities and (d) cycling stability of the device at 2 A g^{-1} .

As shown in our results, the overall electrochemical performances of $\text{MnO}_2@\text{f-VGS}$ composites synthesized using sustainable green resource (*M. alternifolia* extract) are significantly higher than that of the reported composites, which is due to the improved functionalization of f-VGS substrate. Given that $C = \epsilon A/d$ (where ϵ is the electrolyte dielectric constant, A is the electrode surface area accessible to the electrolyte ions, and d is the effective thickness of the double

layer), electrode materials with a larger surface area can provide higher capacitance. Therefore, the exposed edge planes fully covered on the substrate surface for f-VGS sample can be directly accessible to electrolyte ions, providing a large surface area for charge storage, which have been considerably investigated previously ²⁹. In comparison, decreased overall performance of MnO₂@h-GS can be associated with horizontal graphene, covering most of the outer surface of substrate along with a few VGS. Moreover, the inherent and interconnected VGS are capable of preventing the MnO₂ film from agglomeration during GCD measurements, enabling better performance in ion diffusivity. Meanwhile, MnO₂ nanocrystals can just be anchored on the surface of horizontal graphene with little protection and separation of VGS in MnO₂@h-GS composite, resulting in lower supercapacitive properties. As a result, a high density of sharp edge planes on the surface of the open, uniform 3D structure of our f-VGS architecture greatly enhance the specific capacitance.

4. Conclusion

In summary, we report a new synthesis of vertical-aligned graphene nanosheets out of natural essential oil precursor by employing a green, single-step PECVD approach and the demonstration as supercapacitor. Longer growth duration (16 min herein) results in vertical-aligned graphene nanosheets on the Ni foam and correspondingly improved supercapacitive

performance compared with the horizontal graphene obtained from a shorter (4 min) growth. Such VGS serve as a promising substrate for binder-free electrode for supercapacitor as well as potential battery and fuel cell applications. Decoration of the f-VGS with MnO₂ as active material show not only enhanced capacitance but outstanding cyclic stability. The sustainable resource based green synthesis of f-VGS structure thus provides a set of expected features and quality which are suitable for next-generation high performance supercapacitors.

Acknowledgement

This study was supported by NIE AcRF research grant No. RI 7/11 RSR and RI 6/14 RSR provided by National Institute of Education, Nanyang Technological University, Singapore, and Ministry of Education Tier 1 grant (RG98/15).

References

1. L. L. Zhang, R. Zhou and X. S. Zhao, *Journal of Materials Chemistry*, 2010, **20**, 5983-5992.
2. G. Wang, L. Zhang and J. Zhang, *Chemical Society reviews*, 2012, **41**, 797-828.
3. B. You, L. Wang, L. Yao and J. Yang, *Chemical communications*, 2013, **49**, 5016-5018.
4. K. Zhang, L. L. Zhang, X. S. Zhao and J. Wu, *Chemistry of Materials*, 2010, **22**, 1392-1401.
5. Z.-S. Wu, W. Ren, D.-W. Wang, F. Li, B. Liu and H.-M. Cheng, *ACS Nano*, 2010, **4**, 5835-5842.
6. H. Shi, *Electrochimica Acta*, 1996, **41**, 1633-1639.

7. X. Cao, Y. Shi, W. Shi, G. Lu, X. Huang, Q. Yan, Q. Zhang and H. Zhang, *Small*, 2011, **7**, 3163-3168.
8. C. Li and G. Shi, *Nanoscale*, 2012, **4**, 5549-5563.
9. Z. Bo, S. Mao, Z. J. Han, K. Cen, J. Chen and K. K. Ostrikov, *Chemical Society reviews*, 2015, **44**, 2108-2121.
10. L. Jiang, T. Yang, F. Liu, J. Dong, Z. Yao, C. Shen, S. Deng, N. Xu, Y. Liu and H. J. Gao, *Advanced materials*, 2013, **25**, 250-255.
11. Q. Liao, N. Li, H. Cui and C. Wang, *Journal of Materials Chemistry A*, 2013, **1**, 13715-13720.
12. D. H. Seo, Z. J. Han, S. Kumar and K. K. Ostrikov, *Advanced Energy Materials*, 2013, **3**, 1316-1323.
13. H. J. Cho, H. Kondo, K. Ishikawa, M. Sekine, M. Hiramatsu and M. Hori, *Carbon*, 2014, **68**, 380-388.
14. M. Hiramatsu, K. Shiji, H. Amano and M. Hori, *Applied physics letters*, 2004, **84**, 4708-4710.
15. Y. Wu, P. Qiao, T. Chong and Z. Shen, *Advanced materials*, 2002, **14**, 64-67.
16. M. V. Jacob, R. S. Rawat, B. Ouyang, K. Bazaka, D. S. Kumar, D. Taguchi, M. Iwamoto, R. Neupane and O. K. Varghese, *Nano letters*, 2015, **15**, 5702-5708.
17. D. H. Seo, A. E. Rider, S. Kumar, L. K. Randeniya and K. Ostrikov, *Carbon*, 2013, **60**, 221-228.

18. J. Wang, C.-F. Wang and S. Chen, *Angewandte Chemie International Edition*, 2012, **51**, 9297-9301.
19. G. Ruan, Z. Sun, Z. Peng and J. M. Tour, *ACS Nano*, 2011, **5**, 7601-7607.
20. C. Zhu, S. Guo, Y. Fang and S. Dong, *ACS Nano*, 2010, **4**, 2429-2437.
21. Z. Sun, Z. Yan, J. Yao, E. Beitler, Y. Zhu and J. M. Tour, *Nature*, 2010, **468**, 549-552.
22. B. Ouyang, M. V. Jacob and R. S. Rawat, *Materials Research Bulletin*, 2015, **71**, 61-66.
23. L. G. Cançado, A. Jorio, E. M. Ferreira, F. Stavale, C. Achete, R. Capaz, M. Moutinho, A. Lombardo, T. Kulmala and A. Ferrari, *Nano letters*, 2011, **11**, 3190-3196.
24. A. C. Ferrari and D. M. Basko, *Nature nanotechnology*, 2013, **8**, 235-246.
25. S. Chen, J. Zhu, X. Wu, Q. Han and X. Wang, *ACS Nano*, 2010, **4**, 2822-2830.
26. Z. Zhang, F. Xiao, L. Qian, J. Xiao, S. Wang and Y. Liu, *Advanced Energy Materials*, 2014, **4**, 1400064.
27. L. Peng, X. Peng, B. Liu, C. Wu, Y. Xie and G. Yu, *Nano letters*, 2013, **13**, 2151-2157.
28. G. Yu, L. Hu, N. Liu, H. Wang, M. Vosgueritchian, Y. Yang, Y. Cui and Z. Bao, *Nano letters*, 2011, **11**, 4438-4442.
29. D. H. Seo, Z. J. Han, S. Kumar and K. Ostrikov, *Advanced Energy Materials*, 2013, **3**, 1316-1323.